CONFERENCE PRE-PRINT

BAYESIAN DATA FUSION FOR ENHANCED EDGE PLASMA DENSITY PROFILE ESTIMATION IN KSTAR

JAEWOOK KIM, Y.U. NAM, JAYHYUN KIM, Y.H. LEE, J.W. JUHN, JONGHA LEE Korea Institute of Fusion Energy Daejeon, Republic of Korea Email: ijwkim@kfe.re.kr

BIN AHN, Y.-C. GHIM Department of Nuclear and Quantum Engineering, KAIST Daejeon, Republic of Korea

SEHYUN KWAK Max-Planck-Institut für Plasmaphysik Greifswald, Germany

Abstract

Reliable reconstruction of the edge electron density profile is essential for interpreting pedestal transport and stability, quantifying neutral-beam attenuation/deposition, and assessing turbulence/ELM control in tokamaks. We present a Bayesian data-fusion framework for KSTAR that combines beam emission spectroscopy (BES), Thomson scattering (TS), and two-color interferometry (TCI) through a collisional–radiative (CR) forward model of Doppler-shifted D α emission. The edge density is treated as a continuous function on flux space with a Gaussian-process prior, while the TS T_e profile supplies the temperature dependence needed for Maxwellian-averaged rate coefficients in the CR system. The likelihood jointly compares TS pointwise densities, TCI chord integrals, and BES channel intensities predicted after mapping through the measured geometry. Posterior exploration with ensemble MCMC yields uncertainty-quantified profiles that are consistent with all diagnostics and the CR physics and simultaneously infers a single absolute calibration factor for BES. Applied to plasma discharges, adding BES sharpens the pedestal gradient, reduces uncertainty in the steep-edge region, and preserves agreement with TCI path integrals; forward checks show an improved match to the observed BES channel pattern relative to TS+TCI alone. These results indicate that deuterium BES, although designed for fluctuation measurements, can be repurposed to enhance edge-profile estimation when coupled to a CR-based Bayesian inference pipeline.

1. INTRODUCTION

Beam Emission Spectroscopy (BES) measures beam-induced atomic line emission from collisional excitation of neutral-beam atoms, providing high spatial resolution constraints on the edge electron density profile. KSTAR's deuterium BES (DBES) was originally designed for density-fluctuation measurements [1,2], whereas alkali BES and helium BES have been used for profile inference on other devices [3,4]. Despite its fluctuation-focused design, the DBES system on KSTAR can also support edge density-profile inference by adapting methodologies established in alkali and helium BES [5]. This includes coupling absolute-intensity calibration with a validated collisional-radiative forward model and applying appropriate regularization. In steep-gradient edge conditions, however, conventional parametric fits (e.g., modified tanh) constrained only by Thomson scattering (TS) and two-color interferometry (TCI) can be inconsistent with BES intensities predicted by collisional-radiative (CR) modeling, and absolute-calibration uncertainties further limit fidelity. These issues motivate an inference scheme that (i) embraces nonparametric profiles, (ii) embeds a validated forward CR model, and (iii) fuses all measurements within a single probabilistic framework. Complementary diagnostics provide the remaining constraints: TS offers localized n_e and T_e with high spatial resolution [6], while TCI contributes line-integrated density sensitivity [7].

This manuscript develops and applies a Bayesian data-fusion approach that integrates TS, TCI, and deuterium BES via a CR forward model, with a Gaussian-process prior to regularize the edge profile without imposing a fixed parametric shape. The posterior is explored by MCMC to deliver uncertainty-quantified profiles that reconcile all three diagnostics. On KSTAR, the method improves agreement between predicted and observed BES intensities, enhances neutral-beam deposition estimates, and generalizes across operating scenarios including RMP-induced ELM suppression, where it captures toroidal dependence of the edge gradient with RMP phase. Beyond immediate physics gains, the framework lays the groundwork for a surrogate neural model to accelerate inference toward near—real-time use in experiment. The remainder of the paper is organized as follows: Section 2

reviews the diagnostics and CR forward modeling; Section 3 formulates the Bayesian inference; Section 4 presents results on KSTAR; and Section 5 concludes.

2. KSTAR DEUTERIUM BES MODEL

2.1 Deuterium (Hydrogen) collisional-radiative (CR) model

Fast neutral deuterium atoms travel along the beam with speed v_b . At each position s the hydrogenic level populations $\mathbf{N}(s) = [N_1, N_2, N_3, ...]^T$ evolve under collisions with electrons and ions and under spontaneous emission,

$$\frac{d\mathbf{N}}{ds} = \frac{1}{v_b} \left[n_e(s) \mathbf{X}^{(e)}(T_e(s), E_b) + n_i(s) \mathbf{X}^{(i)}(T_i(s), E_b) + \mathbf{\Lambda} \right] \mathbf{N}(s).$$

Matrices $\mathbf{X}^{(e)}$ and $\mathbf{X}^{(i)}$ contain excitation, de-excitation, and ionization rate coefficients for electron and ion impacts. The matrix $\mathbf{\Lambda}$ contains spontaneous decay terms. The neutral manifold is initialized at the beam entrance with $N_1 \approx 1$ and $N_{n>1} \approx 0$, and the system naturally accounts for attenuation through the ionization channels in $\mathbf{X}^{(e,i)}$. The model outputs the population of the n=3 level along the path, and the local D_{α} emissivity density is $\varepsilon_{D_{\alpha}}(s) = A_{32}N_3(s)$, with A_{32} the Einstein coefficient for the $n=3 \rightarrow 2$ transition.

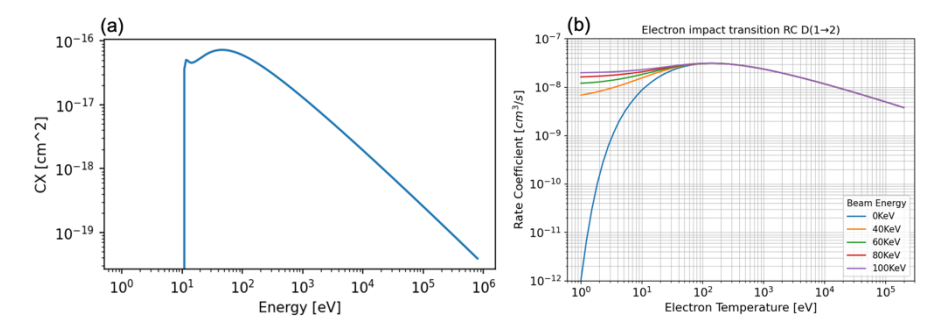


Fig 1. (a) Electron-impact excitation cross-section $\sigma_{1\rightarrow2}^{(e)}(E)$ for deuterium versus electron impact energy E (b) Corresponding Maxwellian-averaged rate coefficient $X_{1\rightarrow2}^e(T_e,E_b)$ versus electron temperature T_e for several beam energies (0, 40, 60, 80, 100 keV)

Two modeling choices simplify the CR system without compromising accuracy for KSTAR DBES. First, once a beam atom is ionized, the resulting charged particle is quickly magnetized and is deflected away from the neutral-beam trajectory by the background magnetic field. On the timescale and geometry of interest, return of these ionized products to the neutral manifold through recombination back into the beam line is negligible. The CR system therefore treats ionization as a true sink from neutral manifold. Second, in the relative collision kinematics for ion impact, the ion thermal speeds are much smaller than the beam speed. It is therefore sufficient to evaluate $\mathbf{X}^{(i)}$ at the beam energy E_b while neglecting the spread associated with T_i ; the ion-impact rates are effectively set by the beam velocity. For example, the electron-impact $1 \to 2$ excitation data are represented by energy-dependent cross section $\sigma_{1\to 2}^{(e)}(E)$ [8], from which Maxwellian-averaged rate $X_{1\to 2}^e(T_e, E_b)$ are constructed; Fig. 1(a) shows $\sigma_{1\to 2}^{(e)}(E)$ versus impact energy, and Fig. 1(b) shows $X_{1\to 2}^e(T_e, E_b)$ versus T_e for several beam energies, summarizing the T_e and E_b dependence adopted in our tables.

The inputs to the CR system are the profile $n_e(s)$ and $T_e(s)$ obtained by mapping flux-coordinate profiles to the beam path, together with the beam energy E_b . Rate coefficients are interpolated from precomputed tables on (T_e, E_b) grids. The ODE is integrated along the chord with a stable explicit or semi-implicit scheme. Conservation of total particle number in the neutral manifold is monitored to detect integration drift. The output is $N_3(s)$ along the path, which feeds the band-integrated forward model.

2.2 Geometry, spatial mapping and spatial sensitivity

Profiles $n_e(\psi)$ and $T_e(\psi)$ are defined on normalized poloidal flux ψ . The beam path is parameterized by arc length s, and an equilibrium reconstruction provides the mapping $s \mapsto \psi_k(s)$ for each sightline segment Δs_k . Spatial registration of the APD array yields channel footprints in the (R, Z) plane as shown in Fig. 2 (a).

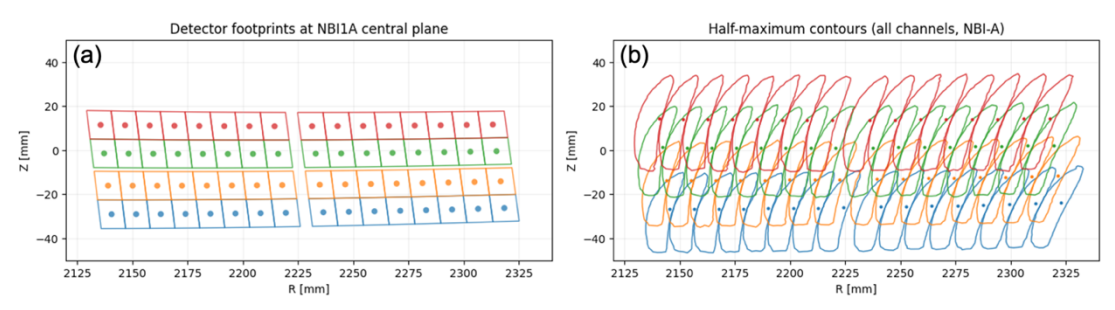


Fig. 2. (a) DBES channel footprints in the (R,Z) plane at the NBI-A central plane. (b) Half-maximum sensitivity contours derived from the footprint extrusion and geometric overlap model.

Each channel is represented by a spatial sensitivity weight $W_k(R,Z)$ in the beam plane rather than by a single point. We obtain W_k by extruding the calibrated image footprint along the viewing direction and integrating its overlap with the beam cross-section over the small toroidal field of view. The resulting, viewaligned elongated shapes have half-maximum envelopes shown in Fig. 2 (b) and exhibit poloidal overlap between neighbors. The beam-path segment Δs_k is then discretized at locations $s_{k,l}$ with arc-length elements $\Delta s_{k,l}$, and the sensitivity weight is sampled along the mapped curve (R(s), Z(s)) to produce metric weights

$$w_{k,l} = \overline{\mathcal{W}}_k\left(R(s_{k,l}), Z(s_{k,l})\right) \Delta s_{k,l}.$$

 $w_{k,l} = \overline{\mathcal{W}}_k\left(R(s_{k,l}), Z(s_{k,l})\right) \Delta s_{k,l}.$ where $\overline{\mathcal{W}}_k$ denotes the weight normalized to unit line-integral along Δs_k , so that $\Sigma_{l \in \Delta s_k} w_{k,l} = 1$. This isolates spatial resolution and channel overlap in $w_{k,l}$ and leaves throughput differences to calibration factors introduced

2.3 Deuterium BES Diagnostic principle

KSTAR's deuterium BES (DBES) measured Doppler-shifted Balmer- α (D α , nominal 656.1 nm) light emitted by fast neutral deuterium atoms in the neutral beam injection as they undergo electron and ion impact excitation followed by radiative decay during beam-plasma interaction. The optical train is intentionally simple: a narrow band-pass filter centred on the expected Doppler-shifted D_{α} transmits a fixed spectral window, relay optics set the collection solid angle and field of view, and an avalanche photodiode (APD) converts the resulting band-integrated photon flux into voltages [9]. Unlike spectrometer-based approaches that fit full line profiles, DBES records a band-integrated intensity per channel; accordingly, the forward model operates on the wavelength-integrated D_{α} emissivity passed by the filter rather than on a per-pixel spectrum.

Let $T_k(\lambda)$ denote the effective passband of channel k (multiplication of filter transmission, optics throughput, and detector quantum efficiency). The photon rate at the detector is

$$\Phi_k = \int_{\Delta S_k} ds \int d\lambda \, T_k(\lambda) \varepsilon_{D_\alpha}(\lambda; s),$$

 $\Phi_k = \int_{\Delta s_k} ds \int d\lambda \, T_k(\lambda) \varepsilon_{D_\alpha}(\lambda;s),$ where, Δ_{s_k} is the path segment intersected by the k-th sightline and ε_{D_α} is the local spectral emissivity. When the D_{α} feature is narrow relative to the filter, we approximate $T_k(\lambda)$ by an effective constant over the transmitted line and write $\varepsilon_{D_{\alpha}}(\lambda;s) \approx \varepsilon_{D_{\alpha}}(s)\phi(\lambda;s)$ with $\int \phi \ d\lambda = 1$, giving $\Phi_k \approx T_k^* \int_{\Delta s_k} \varepsilon_{D_{\alpha}}(s) ds$. However, two effects can shift or broaden the line within the passband: (i) the neutral-beam Doppler shift varies with beam energy for adequate plasma heating, and (ii) the motional Stark effect in the toroidal magnetic field introduces additional broadening/splitting. To render the measurement robust against these spectral details, we normalize using beam-into-gas (BIG) data acquired at nearly the same beam energy and toroidal magnetic field as the plasma shots. This per-channel normalization strongly reduces sensitivity to the exact passband shape $T_{\nu}(\lambda)$ and to the precise line shape $\phi(\lambda; s)$, leaving only a single global scale to be inferred in the BES analysis.

The raw APD output can be written as

$$I_k^{raw} = G_k \Phi_k + b_k + \eta_k$$

 $I_k^{raw} = G_k \Phi_k + b_k + \eta_k$, where G_k is the gain (APD responsivity and electronics) of channel k, b_k represents the background, and η_k captures noise. Under typical KSTAR conditions the background is dominated by plasma bremsstrahlung and is removed in situ using beam blips, which are brief beam-off intervals interleaved with beam-on periods. The background-subtracted signal for blip index t is defined as

$$I_{k,t}^{BES} = I_{k,t}^{on} - I_{k,t}^{off} \approx G_k \Phi_k + \eta_{k,t}$$

 $I_{k,t}^{BES} = I_{k,t}^{on} - I_{k,t}^{off} \approx G_k \Phi_k + \eta_{k,t},$ where $\eta_{k,t}$ collects the uncorrelated noise contributions from the two measurements.

To make the optics explicit before compressing the factors into calibration constants, consider a short element of length Δs at position s. Excited deuterium in n=3 decays to n=2 with rate A_{32} . During acquisition time Δt and for beam particle current I_b the emitted photon number is

$$N_{ph}^{em}(s) = I_b \Delta t \frac{A_{32}}{v_b} \Delta s N_3(s).$$

A fraction T_k of these photons reaches the detector and the APD converts them to voltage with factor G_k , so the contribution from the element is

$$S_k(s) = G_k T_k I_b \Delta t \frac{A_{32}}{v_h} \Delta s \ N_3(s).$$

Summation along Δs_k yields

$$\hat{S}_k = \frac{G_k T_k I_b \Delta t}{v_b} \sum_{l \in \Delta S_k} A_{32} N_3 (s_{k,l}) \Delta s_{k,l}.$$

For calibration, we use BIG shots in a relative sense. Per-channel relative throughput factors \tilde{C}_k^{BIG} , normalized across channels, capture inter-channel differences without fixing the absolute scale. With bandintegrated treatment and BIG normalization, the detector equation reduces to a line integral of the CR emissivity weighted by a per-channel factor. Using $\varepsilon_{D_{\alpha}}(s) = A_{32}N_3(s)$ and discretizing the path with metric weight $w_{k,l}$, the plasma experiment model is

$$\hat{I}_k = \alpha \tilde{C}_k^{BIG} \sum_{l \in \Delta S_k} w_{k,l} A_{32} N_3(s_{k,l}; n_e, T_e, E_b),$$

 $\hat{I}_k = \alpha \tilde{C}_k^{BIG} \sum_{l \in \Delta s_k} w_{k,l} A_{32} N_3(s_{k,l}; n_e, T_e, E_b),$ and the background-subtracted samples satisfy $I_{k,t}^{BES} = \hat{I}_k + \eta_{k,t}$. The single absolute calibration factor α is inferred jointly with the plasma density profile, so the data determine the absolute scale while \tilde{C}_k^{BIG} fixes only the relative gains, and any residual spectral mismatch is absorbed by α and reflected in its posterior uncertainty.

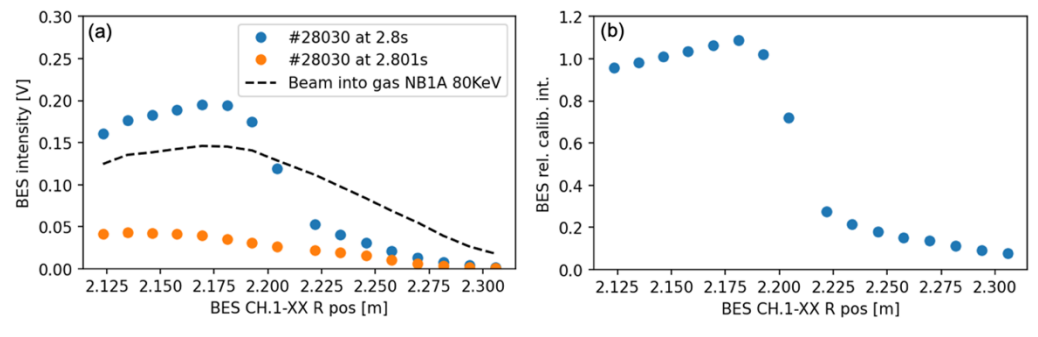


Fig 3. (a) DBES channel signals for a representative plasma shot. Blue markers indicate the beam-on intensities. Orange markers indicate the beam-blip (beam-off) background samples that were acquired 1ms after the corresponding beam-on point. The dashed curve shows a beam-into-gas reference that reveals the inter-channel throughput trend. (b) Background-subtracted and relatively calibrated DBES intensities across the channel array.

As an example, Fig. 3 (a) illustrates a representative discharge: blue markers show the beam-on DBES intensities, orange markers are the beam-blip (beam-off) background samples acquired 1ms after the beam-on point, and the dashed curve is a beam-into-gas reference that reveals the inter-channel throughput trend. Using the orange beam-off points as I^{off} , we subtract the background and then apply a relative inter-channel calibration (guided by the beam-into-gas pattern); the resulting channel-normalized profile is shown in Fig. 3 (b). These steps decouple the background level from the inter-channel response, yielding inputs directly comparable to the bandintegrated CR forward model.

BAYESIAN INFERENCE AND DATA FUSION

3.1 Bayes' rule and hierarchical formulation

The inference begins from Bayes' rule, which updates prior knowledge of the electron-density profile and calibration into a posterior distribution conditioned on all observations. Let y denote the concatenated data vector, let $f(\psi)$ be the continuous profile on normalized poloidal flux coordinate, and let α be the single absolute DBES calibration factor that remains after beam-into-gas normalization. The posterior is

$$p(\mathbf{f}, \alpha | \mathbf{y}) \propto p(\mathbf{y} | \mathbf{f}, \alpha) p(\alpha) p(\mathbf{f}).$$

The likelihood gathers the processed Thomson-scattering and tangential interferometer products with the CR-based DBES forward model; for DBES we infer a single absolute calibration factor α jointly with the profile. We explore the posterior with emcee, an ensemble sampler that advances many walkers concurrently, enabling straightforward parallelization.

3.2 Likelihood formulation: TS/TCI processed data and DBES forward model

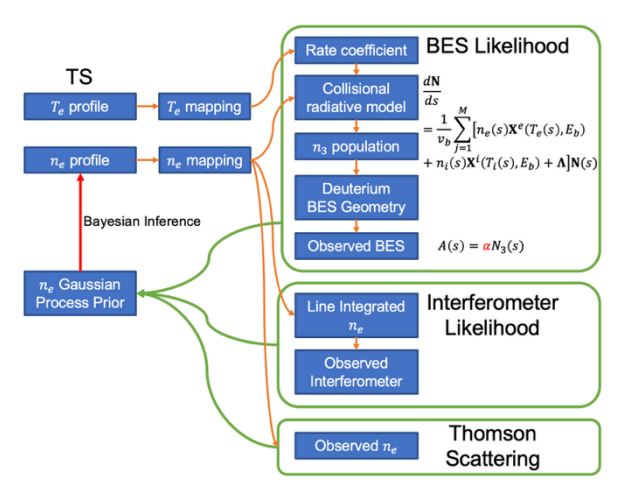


Fig. 4. Graphical summary of the Bayesian data-fusion forward model. TS provides T_e for rate coefficients and constrains n_e which is mapped to the beam, evolved with the CR model to $N_3(R)$, and projected through the BES geometry to predict band-integrated DBES signals with an absolute factor α . The same n_e is line-integrated to

We begin by summarizing the forward map that connects the unknown electron-density profile and the measured diagnostics. Fig. 4 provides a graphical representation of the pipeline used in the inference. The Thomson-scattering T_e profile is mapped to the beam path and supplies the Maxwellian-averaged rate coefficients. The unknown $n_e(\psi)$ endowed with a Gaussian-process prior and mapped along the beam, drives the collisional–radiative ODE to yield the n = 3population $N_3(s)$. The deuterium BES geometry projects N_3 into channel space, and a single absolute factor α sets the overall band-integrated DBES scale. In parallel, the same n_e profile is line-integrated along interferometer chords to compare with measurements.

The TS and TCI measurements enter through processed-data likelihoods that compare the model predictions for the continuous profile directly to the already reconstructed data products delivered by each system. The processed TS vector y_{TS} contains channelwise electron-density estimates at mapped flux locations together with their reported uncertainties. The

processed TCI vector y_{TCI} contains path-integrated density estimates per chord with their reported uncertainties. The DBES signal is generated by the CR forward operator \mathcal{F} that integrates the neutral manifold along the mapped beam path, forms the population N_3 , converts it to the wavelength-integrated D_{α} emissivity, and projects the result onto each channel through the measured spatial weights with beam-into-gas normalization fixing relative throughputs. DBES provides band-integrated intensities per sightline that are formed from high-rate samples within a selected time window. For each channel k the mean \bar{I}_k over the window is taken as the measurement and the associated variance is the standard error of the mean, s_k^2/N_K , where s_k is sample standard deviation about \bar{I}_k and N_K is the number of samples in the window, so that intrinsic fluctuations contribute to the uncertainty. The joint observation model is

$$\begin{bmatrix} y_{TS} \\ y_{TCI} \\ y_{DBES} \end{bmatrix} = \begin{bmatrix} \mathcal{H}_{TS}f \\ \mathcal{L}_{TCI}f \\ \mathcal{F}(f,\alpha) \end{bmatrix} + \varepsilon, \quad \varepsilon \sim \mathcal{N}(0,\Sigma).$$

The covariance Σ is block diagonal with Σ_{TS} , Σ_{TCI} , Σ_{DBES} and permits heteroscedastic noise across diagnostics. The corresponding likelihood factors are

$$\begin{aligned} p(y_{TS}|f) &= \mathcal{N}(y_{TS}; \mathcal{H}_{TS}f, \Sigma_{TS}), \\ p(y_{TCI}|f) &= \mathcal{N}(y_{TCI}; \mathcal{L}_{TCI}f, \Sigma_{TCI}), \\ p(y_{DBES}|f) &= \mathcal{N}(y_{DBES}; \mathcal{F}(f, \alpha), \Sigma_{DBES}). \end{aligned}$$

The operator $\mathcal{F}(f,\alpha)$ integrates the CR ODE along each mapped sightline using $n_e(\psi) = f(\psi)$ and tabulated rate coefficient to obtain $N_3(s)$ projects to each channel through the measured spatial sensitivity weights and the relative throughputs from beam-into-gas and finally applies the absolute calibration factor α .

3.3 Gaussian-process prior and posterior computation

Regularization of the continuous profile is provided by a Gaussian-process prior that remains nonparametric while encoding physically sensible smoothness. The prior is

$$f \sim \mathcal{GP}(m(\psi), k(\psi, \psi')),$$

where we set $m(\psi) = 0$ expresses that departures from zero and the kernel k implements nonstationary correlation consistent with core-edge scale separation. The local correlation length $l(\psi)$ is prescribed from pretraining or channel geometry and remains fixed during inference, with a convenient closed form given by the Gibbs (nonstationary) kernel [9-11]:

$$k(\psi, \psi') = \sigma_f^2 \sqrt{\frac{2l(\psi)l(\psi')}{l^2(\psi) + l^2(\psi')}} \exp\left[-\frac{(\psi - \psi')^2}{l^2(\psi) + l^2(\psi')}\right],$$

so that σ_f and $l(\psi)$ are not sampled. Under this choice the unknowns are the discretized values of $f(\psi)$ on a moderate grid together with the scalar α . We employ the affine-invariant ensemble sampler [12] via emcee, a Python package [13], to sample the joint space of the discretized f and the scalar α ; multiple walkers are launched and updated in parallel.

3.4 TS/TCI-only comparison baseline

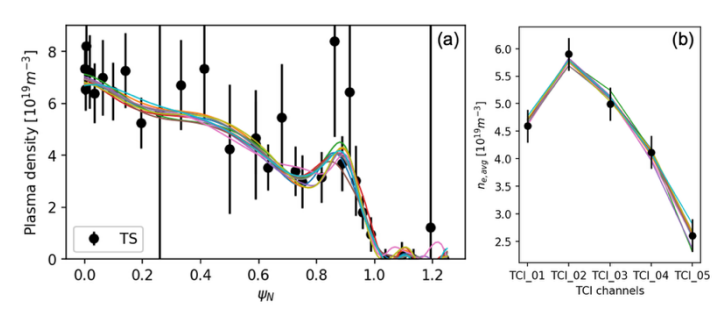


Fig. 5. (a) It overlays ten posterior samples of $f(\psi_N)$ on the processed TS points (black markers with their processing-derived error bars), showing that the TS-anchored profile remains smooth between channels under the GP prior. (b) It shows the ten posterior-predictive TCI curves $\mathcal{L}_{TCI}f$ computed from the same draws, compared against the processed TCI values with their reported error bars.

To establish a baseline independent of DBES, we infer the profile $f(\psi_N)$ using only the processed-data likelihoods for Thomson scattering and tangential interferometry. The posterior is

 $p(f|y_{TS}, y_{TCI}) \propto p(y_{TS}|f)p(y_{TCI}|f)p(f)$, with the zero-mean Gaussian-process prior and fixed hyperparameter described above. Sampling uses emcee over the discretized f with multiple walkers in parallel. Fig. 5 visualizes ten posterior draws and their TCI predictions.

4. EDGE-REGION IMPROVEMENTS FROM DBES-INFORMED BAYESIAN INFERENCE

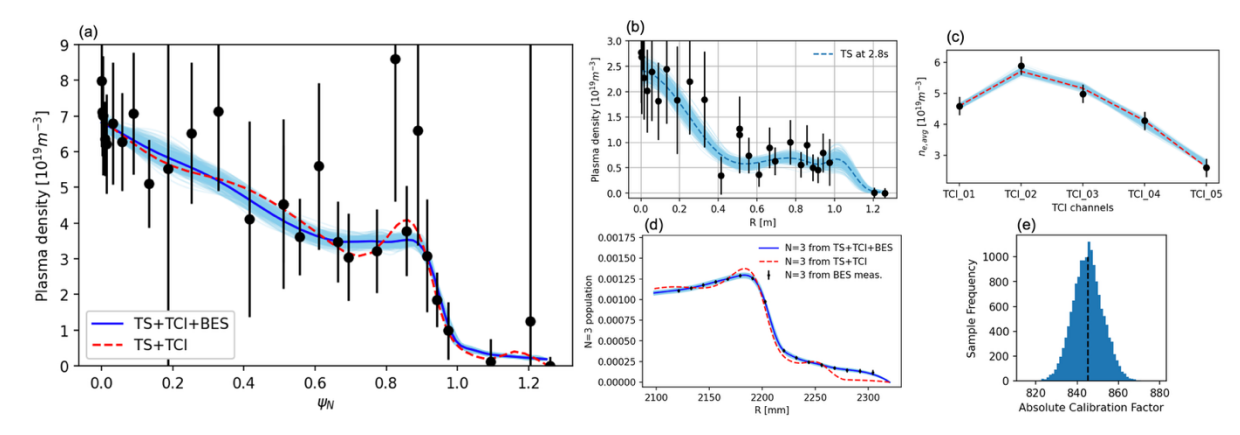


Fig. 6. It presents the Bayesian data-fusion results for a representative KSTAR discharge. Panel (a) shows the inferred electron-density profile versus normalized poloidal flux ψ_N compared with TS measurements; the TS+TCI+BES posterior (blue with shading) features a sharper edge and narrower uncertainty than the TS+TCI result (red dashed). Panel (b) displays the TS electron-temperature profile and its smooth fit used as input to the CR operator. Panel (c) compares predicted TCI chord integrals from both posteriors with the TCI data and shows agreement within uncertainties. Panel (d) evaluates the CR forward model along the beam and indicates that the TS+TCI+BES solution better reproduces the observed BES channel pattern. Panel (e) summarizes the posterior distribution of the absolute BES calibration factor α .

We evaluate two inference configurations on the same discharge: a baseline that fuses Thomson scattering (TS) with the tangential interferometer (TCI), and a fully fused case that adds band-integrated deuterium BES through the collisional–radiative (CR) operator. The temperature profile required by the CR model is taken from TS and smoothly fitted to provide a noise-robust input; the absolute BES calibration factor α is sampled jointly with the electron-density profile. Fig. 6 (a) compares the inferred density profiles against the TS measurements

with uncertainties. The TS+TCI posterior (red dashed) already follows the overall trend, but the addition of BES (blue with shading) sharpens the edge gradient and reduces the credible-band width near the separatrix while leaving the core essentially unchanged. This behavior indicates that the band-integrated BES constraint is most informative where the pedestal is steep and TS spatial sampling alone can under-resolve rapid variations.

To run the CR forward model, we use the fitted TS temperature profile shown in Fig. 6 (b), which supplies the T_e dependence needed to evaluate Maxwellian-averaged rate coefficients. Consistency checks against line-integrated constraints appear in Fig. 6 (c): chord integrals predicted from both posteriors agree with the TCI measurements within their reported uncertainties, showing that the BES-driven sharpening at the edge remains compatible with the path-integrated density. A complementary check along the neutral-beam path is shown in Fig. 6 (d). Here the TS+TCI+BES solution reproduces the measured channel pattern more closely than the TS+TCI baseline across the region of strongest signal, demonstrating that the fused posterior reconciles the DBES intensities without degrading agreement elsewhere. Finally, Fig. 6 (e) displays the posterior samples of the

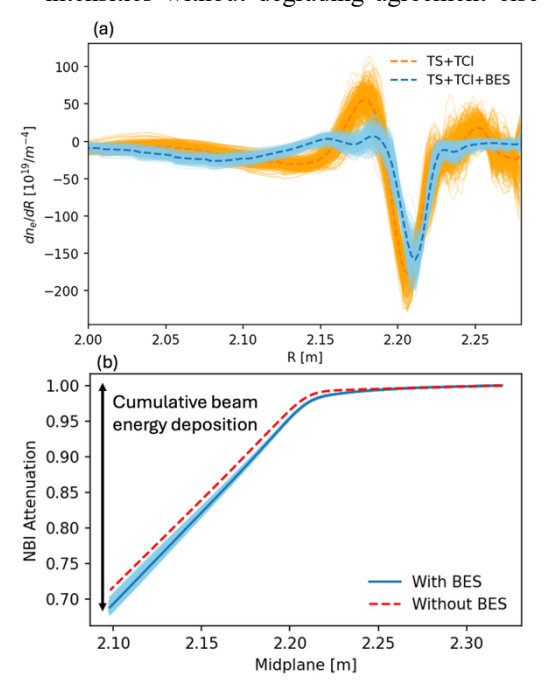


Fig. 7. (a) Density gradient dn_e/dR inferred from Thomson scattering with the interferometer, with and without adding BES; including BES sharpens the edge peak and narrows the uncertainty. (b) Cumulative neutral-beam attenuation along the midplane for the same two configurations; including BES yields slightly stronger early attenuation

absolute calibration factor α . The distribution is unimodal and reasonably narrow, implying that the joint data provide enough information to determine the absolute scale while relative interchannel response is handled separately. Overall, incorporating BES primarily impacts the pedestal and near-edge region, tightening uncertainties where gradients are largest and improving agreement with the measured BES channel dependence, all while preserving consistency with TS and TCI data.

Fig. 7 further quantifies how the fused constraint modifies edge physics. Panel (a) plots the posterior gradient dn_a/dR obtained first from the configuration that combines Thomson scattering with the tangential interferometer, and then from the configuration that additionally incorporates beam-emission spectroscopy through the CR operator. Including BES tightens the uncertainty envelope across the pedestal and yields a steeper, more localized gradient peak near the separatrix, while the broader-core shear remains essentially unchanged. This behavior is consistent with the profile-level results in Fig. 6 and indicates that BES information is most impactful where the edge varies rapidly and the spatial sampling of Thomson scattering alone can under-resolve structure. Panel (b) shows the corresponding cumulative neutral-beam attenuation along the midplane inferred from each configuration. When BES is included, the attenuation becomes slightly stronger in the core region, reflecting increased local ionization and earlier power deposition. The narrower uncertainty band with BES implies more reliable deposition estimates without sacrificing consistency with interferometer chord integrals.

5. SUMMARY

Embedding a deuterium collisional–radiative (CR) forward operator in a nonparametric Bayesian inversion and assimilating TS, TCI, and band-integrated DBES yields edge density profiles that are diagnostically consistent and uncertainty-quantified. Channel-dependent optics are handled through measured spatial sensitivity weights and BIG relative throughput, while a single absolute BES scale α is inferred with the profile; the posterior for α is unimodal and sufficiently narrow to set the overall scale without over-constraining shape.

Relative to a TS+TCI baseline, the fused posterior sharpens the pedestal gradient and contracts credible intervals near the separatrix while leaving core structure essentially unchanged. The predicted DBES channel pattern aligns more closely with observations across the high-signal region, and line-integrated predictions remain within TCI uncertainties. These improvements translate into more reliable estimates of neutral-beam attenuation and deposition and reproduce toroidal edge-gradient variations with RMP phase, indicating cross-diagnostic coherence in regimes including ELM suppression.

[Right hand page running head is the paper number in Times New Roman 8 point bold capitals, centred]

Methodologically, the framework replaces fixed-form fits with a physics-informed, nonparametric prior that regularizes with spatially varying length scales. Heteroscedastic noise is retained at the likelihood level, so posterior bands reflect both measurement scatter and model sensitivity. Ensemble MCMC over the discretized profile and α showed stable convergence; keeping GP hyperparameters and geometric weights fixed constrained the parameter space without masking edge structure in tested cases. The remaining practical limitation is computational cost: posterior exploration with ensemble MCMC is too slow for experiment-time use. We therefore plan to train a surrogate neural model of the CR operator (and its embedding in the likelihood) to amortize inference and deliver near-real-time profile estimates.

Overall, the data-fusion approach delivers sharper, better-constrained edge profiles, improves neutral-beam deposition inference, offering immediate utility for post-shot analysis and a concrete path toward accelerated, experiment-time profile estimation for control and turbulence studies.

ACKNOWLEDGEMENTS

This research was supported by R&D Program of "High Performance Tokamak Plasma Research & Development (code No. EN2501-16)" through the Korea Institute of Fusion Energy (KFE) funded by the Government funds, Republic of Korea.

REFERENCES

- [1] NAM, Y. U., ZOLETNIK, S., LAMPERT, M., KOVÁCSIK, Á., Analysis of edge density fluctuation measured by trial KSTAR beam emission spectroscopy system, Rev. Sci. Instrum. 83 10 (2012) 10D531.
- [2] NAM, Y. U., ZOLETNIK, S., LAMPERT, M., KOVÁCSIK, Á., WI, H. M., Edge electron density profiles and fluctuations measured by two-dimensional beam emission spectroscopy in the KSTAR, Rev. Sci. Instrum. 85 (2014) 11E434.
- [3] WILLENSDORFER, M., BIRKENMEIER, G., FISCHER, R., LAGGNER, F. M., WOLFRUM, E., VERES, G., et al., Characterization of the Li-BES at ASDEX Upgrade, Plasma Phys. Control. Fusion 56 2 (2014) 025008.
- [4] ZOLETNIK, S., HU, G. H., TÁL, B., DUNAI, D., ANDA, G., ASZTALOS, O., POKOL, G. I., KÁLVIN, S., NÉMETH, J., KRIZSANÓCZI, T., Ultrafast two-dimensional lithium beam emission spectroscopy diagnostic on the EAST tokamak, Rev. Sci. Instrum. 89 6 (2018) 063503.
- [5] KWAK, S., SVENSSON, J., BRIX, M., GHIM, Y.-C., and JET CONTRIBUTORS, Bayesian electron density inference from JET lithium beam emission spectra using Gaussian processes, Nucl. Fusion 57 (2017) 036017.LEE, J. H., OH, S. T., WI, H. M., Development of KSTAR Thomson scattering system, Rev. Sci. Instrum. 81 10 (2010) 10D528.
- [6] JUHN, J.-W., LEE, K. C., LEE, T. G., WI, H. M., KIM, Y. S., HAHN, S. H., NAM, Y. U., Multi-chord IR-visible twocolor interferometer on KSTAR, Rev. Sci. Instrum. 92 4 (2021) 043559.
- [7] JANEV, R. K., REITER, D., SAMM, U., Collision Processes in Low-Temperature Hydrogen Plasmas, internal report, Forschungszentrum Jülich GmbH, Jülich (2003). Report No. JUEL-4105.
- [8] LAMPERT, M., ANDA, G., CZOPF, A., ERDEI, G., GUSZEJNOV, D., KOVÁCSIK, Á., POKOL, G. I., RÉFY, D., NAM, Y. U., ZOLETNIK, S., Combined hydrogen and lithium beam emission spectroscopy observation system for Korea Superconducting Tokamak Advanced Research, Rev. Sci. Instrum. 86 7 (2015) 073501.
- [9] KWAK, S., SVENSSON, J., BOZHENKOV, S., FLANAGAN, J., KEMPENAARS, M., BOBOC, A., GHIM, Y.-C., and JET CONTRIBUTORS, Bayesian modelling of Thomson scattering and multichannel interferometer diagnostics using Gaussian processes, Nucl. Fusion 60 (2020) 046009.
- [10] CHILENSKI, M. A., GREENWALD, M., MARZOUK, Y., HOWARD, N. T., WHITE, A. E., RICE, J. E., WALK, J. R., Improved profile fitting and quantification of uncertainty in experimental measurements of impurity transport coefficients using Gaussian process regression, Nucl. Fusion 55 (2015) 023012.
- [11] GIBBS, M. N., Bayesian Gaussian processes for regression and classification, PhD Thesis, University of Cambridge
- [12] GOODMAN, J., WEARE, J., Ensemble samplers with affine invariance, Commun. Appl. Math. Comput. Sci. 5 1 (2010)
- [13] FOREMAN-MACKEY, D., HOGG, D. W., LANG, D., GOODMAN, J., emcee: The MCMC Hammer (2013).